NIR and Magnetism Dual-Response Multi-core Magnetic Vortex Nanoflowers for Boosting Magneto-photothermal Cancer Therapy

Kaiming Shen[1], Lixian Li[2*], Funan Tan[3], Calvin Ching lan Ang[3], Tianli Jin[3], Zongguo Xue[1], Mun Yin Chee[3], Yunfei Yan[1*], Wen Siang Lew [3*]

[1]Key Laboratory of Low-grade Energy Utilization Technologies and Systems, Chongqing University, Chongqing 400044, China

[2]Department of Pharmacy, Chongqing University Cancer Hospital, Chongqing 400030, China

[3]School of Physical and Mathematical Sciences, Nanyang Technological University,

21 Nanyang Link, Singapore 637371

METHODS/EXPERIMENTAL

Chemical. Ferric chloride hexahydrate ($FeCl_3 \cdot 6H_2O$), zinc chloride ($ZnCl_2$), tetrahydrate manganese chloride ($MnCl_2 \cdot 4H_2O$), ethylene glycol (EG), sodium acetate (CH_3COONa), hexadecyl trimethyl ammonium bromide (CTAB), acetone (C_3H_6O), N-hydroxysuccinimide (NHS), 1-ethyl-3-(3-dimethyl aminopropyl) carbodiimide (EDC), NH_2-PEG-NH_2, and urea (CH_4N_2O) were obtained from Shanghai Aladdin Industrial Corporation, Shanghai China. Human breast cancer cells (MCF-7, BT549), and mouse cells (4T1) were cultured in Dulbecco's modified Eagle medium (DMEM) supplemented with 10% fetal bovine serum (FBS), 1% penicillin/streptomycin at 37 °C in an atmosphere with 100% humidity, and 5% CO_2. FBS and DMEM were obtained from Shanghai Beyotime Biotechnology Co., Ltd., Shanghai, China. Calcein-AM, lysobrite green, propidium iodide (PI), and methyl thiazolyl tetrazolium (MTT) were obtained from Shanghai Beyotime Biotechnology Co., Ltd., Shanghai China. All chemicals and reagents were of analytical grade and used without any further purification.

1*Corresponding email address: yunfeiyan@cqu.edu.cn (Y. Yan)

2*Corresponding email address: lilixian@cqu.edu.cn (L. Li)

3*Corresponding email address: wensiang@ntu.edu.sg

Synthesis of Cubic Mn$_{0.5}$Zn$_{0.5}$Fe$_2$O$_4$-PEG

The synthesis procedure of the cubic Mn$_{0.5}$Zn$_{0.5}$Fe$_2$O$_4$-PEG is as follows: first, FeCl$_3$·6H$_2$O (1.08 g), ZnCl$_2$ (0.13 g), and MnCl$_2$·4H$_2$O (0.198 g) were dissolved in 60mL EG under magnetic stirring until a homogenous liquid was obtained. Then, the NaOH (2.4 g) were added and stirred for 15 min at 90 °C until it became completely transparent. Next, the mixture was transferred into the Teflon autoclave for the solvothermal process, and heated at different temperature (180 °C) for 12 h. Following cooling to room temperature, the resulting black solution underwent multiple washes with ethanol and deionized water before being dried overnight at 60 °C under vacuum conditions. The as-prepared cubic Mn$_{0.5}$Zn$_{0.5}$Fe$_2$O$_4$ nanoparticles were modified with PEG-bis-amine. Briefly, 15 mg Mn$_{0.5}$Zn$_{0.5}$Fe$_2$O$_4$ nanoparticles were ultrasound dispersed into 20 mL deionized water, then incubated with 250 μL 100 mg mL^{-1} EDCI and 200 μL 100 mg mL^{-1} NHS, and stirring vigorously for 30 min at room temperature. Subsequently, the resulting NHS-activated nanoparticles were covalently linked to NH$_2$-PEG-NH$_2$ (300 μL 100 mg mL^{-1}) at room temperature by stirring for 6 h, and then dried at 60 °C in a vacuum for 12 h.

Synthesis of Hollow Spherical Mn$_{0.5}$Zn$_{0.5}$Fe$_2$O$_4$-PEG

The synthesis procedure of the hollow spherical Mn$_{0.5}$Zn$_{0.5}$Fe$_2$O$_4$-PEG is as follows: first, FeCl$_3$·6H$_2$O (1.08 g), ZnCl$_2$ (0.13 g), and MnCl$_2$·4H$_2$O (0.198 g) were dissolved in 60mL EG under magnetic stirring until a homogenous liquid was obtained. Then, the different amount of Urea (1.45 g, 24 mmol; 1.92 g, 32 mmol; 2.4 g, 40 mmol) and CTAB (2.18 g, 6 mmol) were added and stirred for 15 min at 90 °C until it became completely transparent. Next, the mixture was transferred into the Teflon autoclave for the solvothermal process, and heated at different temperature (180 °C, 200 °C, 220 °C) for 24 h. Following cooling to room temperature, the resulting black solution underwent multiple washes with ethanol and deionized water before being dried overnight at 60 °C under vacuum conditions. Finally, the CTAB was removed by acetone reflux at 85 °C to get the pure hollow spherical Mn$_{0.5}$Zn$_{0.5}$Fe$_2$O$_4$.

The as-prepared hollow spherical Mn$_{0.5}$Zn$_{0.5}$Fe$_2$O$_4$ nanoparticles were modified with PEG-bis-amine. Briefly, 15 mg Mn$_{0.5}$Zn$_{0.5}$Fe$_2$O$_4$ nanoparticles were ultrasound dispersed into 20 mL deionized water, then incubated with 250 μL 100 mg mL^{-1} EDCI and 200 μL 100 mg mL^{-1} NHS, and stirring vigorously for 30 min at room temperature. Subsequently, the resulting NHS-activated

nanoparticles were covalently linked to NH_2-PEG-NH_2 (300 μL 100 mg mL^{-1}) at room temperature by stirring for 6 h, and then dried at 60°C in a vacuum for 12 h.

Preparation of $Mn_{0.5}Zn_{0.5}Fe_2O_4$-PEG with ellipsoidal magnetic cores nanoflowers (MZF-NFE). $Mn_{0.5}Zn_{0.5}Fe_2O_4$ nanoparticles were synthesized using the solvothermal method. First, $FeCl_3 \cdot 6H_2O$ (2.16 g, 8 mmol), $ZnCl_2$ (0.26 g, 2 mmol), and $MnCl_2 \cdot 4H_2O$ (0.39 g, 2 mmol) were dissolved in 60 mL EG under magnetic stirring until a homogenous liquid was obtained. Then, CH_3COONa (15 mmol) and CTAB (12 mmol) were added and stirred for 15 min at 90°C. Finally, the mixture was poured into the 100 mL Teflon autoclave, and heated at 200°C for 24 h. After cooling to room temperature, the product was washed 6 times with ethanol and deionized water and then dried at 60°C in a vacuum for 12 h to obtain $Mn_{0.5}Zn_{0.5}Fe_2O_4$-CTAB. Finally, the CTAB was removed by acetone reflux at 85°C to obtain the $Mn_{0.5}Zn_{0.5}Fe_2O_4$ multicore nanoflowers with large magnetic cores.

The $Mn_{0.5}Zn_{0.5}Fe_2O_4$ nanoparticles were modified with PEG-bis-amine. Briefly, 15 mg $Mn_{0.5}Zn_{0.5}Fe_2O_4$ nanoparticles were dispersed in ultrasound in 20 mL of deionized water, then incubated with 250 μL 100 mg mL^{-1} EDCI and 200 μL 100 mg mL^{-1} NHS for 30 min at room temperature with gentle stirring. The resulting NHS-activated nanoparticles were then covalently linked to NH_2-PEG-NH_2 (300 μL 100 mg mL^{-1}) at room temperature stirring for 6 h and then dried at 60 °C in a vacuum for 12 h to obtain the $Mn_{0.5}Zn_{0.5}Fe_2O_4$-PEG.

Preparation of $Mn_{0.5}Zn_{0.5}Fe_2O_4$ with needle-like magnetic cores nanoflowers (MZF-NFN)

$Mn_{0.5}Zn_{0.5}Fe_2O_4$ nanoparticles were synthesized using the solvothermal method. First, $FeCl_3 \cdot 6H_2O$ (2.16 g, 8 mmol), $ZnCl_2$ (0.26 g, 2 mmol), and $MnCl_2 \cdot 4H_2O$ (0.39 g, 2 mmol) were dissolved in 60 mL EG under magnetic stirring until a homogenous liquid was obtained. Then, CH_3COONa (15 mmol) and CTAB (12 mmol) were added and stirred for 15 min at 90 °C. Finally, the mixture was poured into the 50 mL Teflon autoclave, and heated at 200°C for 24 h. After cooling to room temperature, the product was washed 6 times with ethanol and deionized water and then dried at 60 °C in a

vacuum for 12 h to obtain $Mn_{0.5}Zn_{0.5}Fe_2O_4$-CTAB. Finally, the CTAB was removed by acetone reflux at 85 °C to obtain the $Mn_{0.5}Zn_{0.5}Fe_2O_4$ with needle-like magnetic cores.

The $Mn_{0.5}Zn_{0.5}Fe_2O_4$ nanoparticles were modified with PEG-bis-amine. Briefly, 15 mg $Mn_{0.5}Zn_{0.5}Fe_2O_4$ nanoparticles were dispersed in ultrasound in 20 mL of deionized water, then incubated with 250 μL 100 mg mL^{-1} EDCI and 200 μL 100 mg mL^{-1} NHS for 30 min at room temperature with gentle stirring. The resulting NHS-activated nanoparticles were then covalently linked to NH_2-PEG-NH_2 (300 μL 100 mg mL^{-1}) at room temperature stirring for 6 h and then dried at 60 °C in a vacuum for 12 h to obtain the $Mn_{0.5}Zn_{0.5}Fe_2O_4$-PEG.

Magneto-photothermal heating Measurements. Magnetic hyperthermia experiments were performed by a calorimetric method using an AC magnetic field generator device under different amplitudes of magnetic field, H (6.4 kA/m – 7.2 kA/m) at a constant frequency of 300 kHz. Photothermal was induced by a near-infrared continuous laser at 808 nm with power densities ranging from 0.3 to 1.0 W/cm^2. Measurements were carried out in an aqueous solution with different sample concentrations (0.5 - 3 mg mL^{-1}) for 600 s while the magnetic hyperthermia and photothermal effects were applied. The elevated temperature was measured by an optical fiber thermometer, and specific absorption rate (SAR) was calculated. Schematic diagram of the photothermal and magnetic hyperthermia is shown in Fig. S1 (Supplementary Information).

Cell culture, biocompatibility, uptake, and cytotoxicity assay. The MCF-7, BT549, and 4T1 cells were cultured in Dulbecco's modified Eagle medium (DMEM) supplemented with 10% (V/V) fetal bovine serum (FBS), 1% penicillin/streptomycin at 37°C in an atmosphere with 100% humidity, and 5% CO_2. The cells were subcultured regularly using trypsin/EDTA.

The MCF-7, BT549, and 4T1 cells were used to evaluate the biocompatibility of MZF-NFE-PEG. First, the MCF-7, BT549, and 4T1 cells were dispensed onto a 96-well plate at a density of 1×10^4 cells/well. After being cultured for 24 h for cell attachment, the media were taken out from the wells, followed by washing three times

with PBS and then incubated with various concentrations of MZF-NFE-PEG (0, 20, 50, 100, and 200 μg/mL). After further incubation for 24 h and 48 h to act as control groups, the solutions were replaced with fresh DMEM, and the cell viability was determined by a standard MTT assay.

For carrying out cell uptake experiments, DOX labeled MZF-NFE-PEG (MZF-NFE-PEG/ DOX) was prepared and the DOX was loaded in MZF-NFE-PEG. MCF-7 and BT549 cells were seeded onto a laser confocal petri dish (Φ = 20 mm) with a density of 2×10^5 cells/well and cultured overnight. The MZF-NFE-PEG/ DOX (DOX = 15 μM) was incubated with the cells at 37 °C for 2 h. After washing 3 times, the cells were stained with Hoechst 33342 (10 μg/mL) and LysoBrite Green (1 μM) in DMEM at 37 °C for 20 min. After washing with PBS 3 times, the cells were observed using a Zeiss LSM800 confocal microscope.

The MCF-7, BT549, and 4T1 cells were seeded onto a laser confocal petri dish at a density of 2×10^5 cells/well and cultured for 24 hr. The three type cells were first incubated with various concentrations of MZF-NFE-PEG (0, 50, 100, 200, 500, and 1000 μg/mL) for 4 hr. After washing with PBS several times and being replaced with fresh DMEM, the cells were kept under both an AMF with an amplitude of 6.7 kA/m and a NIR of 0.5 W/cm^2 for 10 min. After the dual-model treatment, the cells were incubated with fresh DMEM containing 10% FBS at 37°C for 30 min. The cells were stained by propidium iodide (PI) and calcein-AM to label live and dead cells respectively and then observed by a fluorescent inverted microscope to evaluate the therapeutic efficacy. The cell survival efficiency of the dual-mode treatment was also further investigated using an MTT assay.
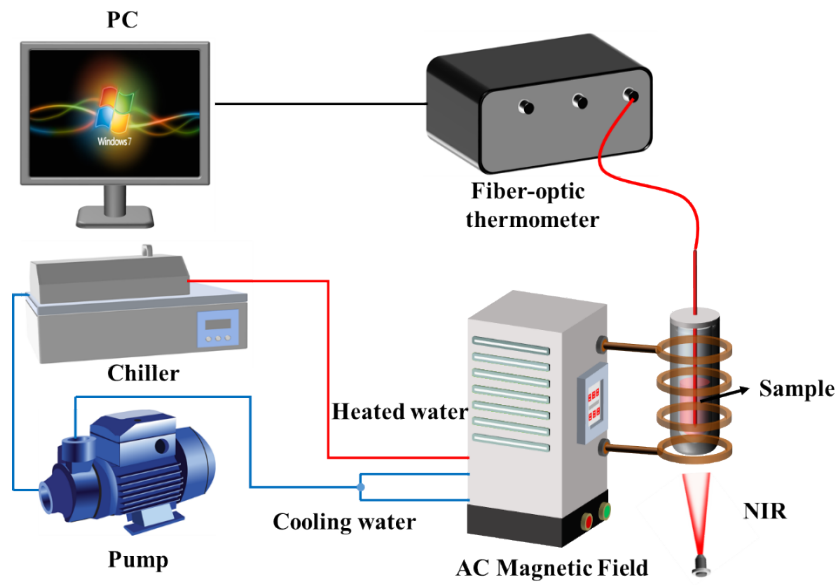
Fig. S1 The schematic diagram of the photothermal and magnetic hyperthermia experiment.
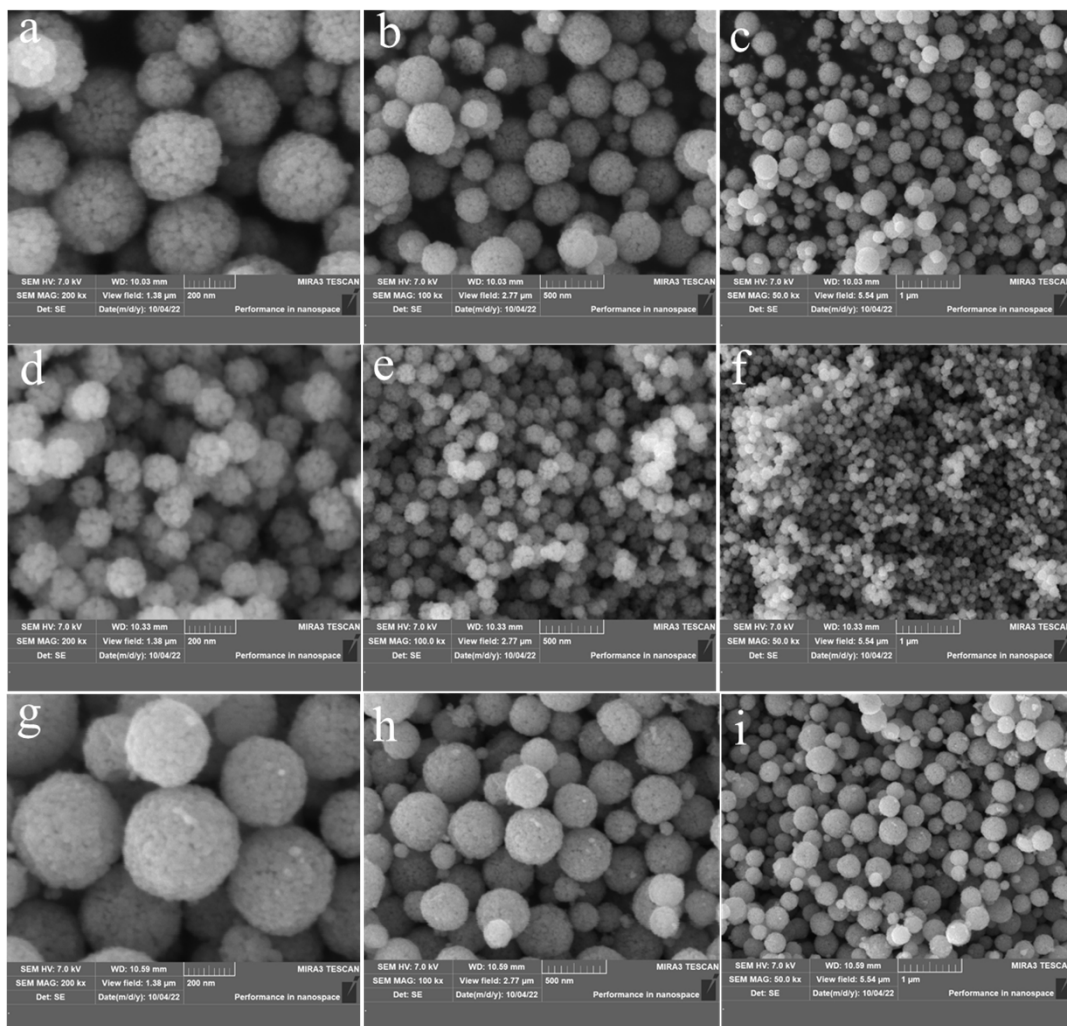

Fig. S2 SEM images of MZF-NFN-PEG NFs (10 mmol NaAc) magnified (a) 200 nm, (b) 500 nm,

and (c) 1 μm. SEM images of MZF-NFE-PEG NFs (15 mmol NaAc) magnified (d) 200 nm, (e) 500 nm, and (f) 1 μm. SEM images of MZF-NFN-PEG NFs (20 mmol NaAc) magnified (g) 200 nm, (h) 500 nm, and (i) 1 μm.
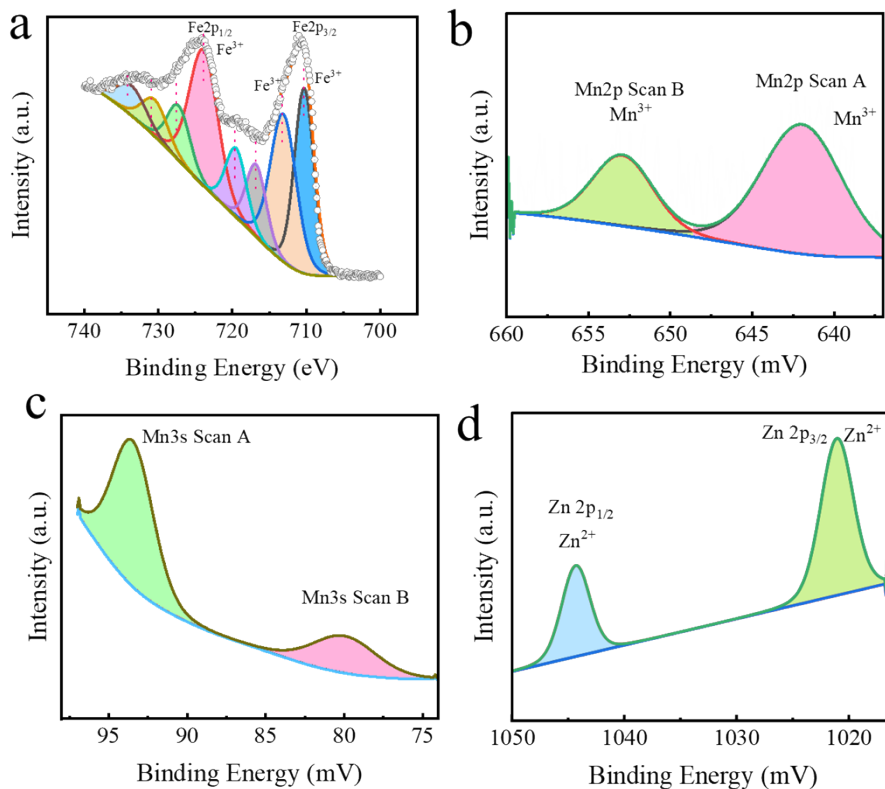

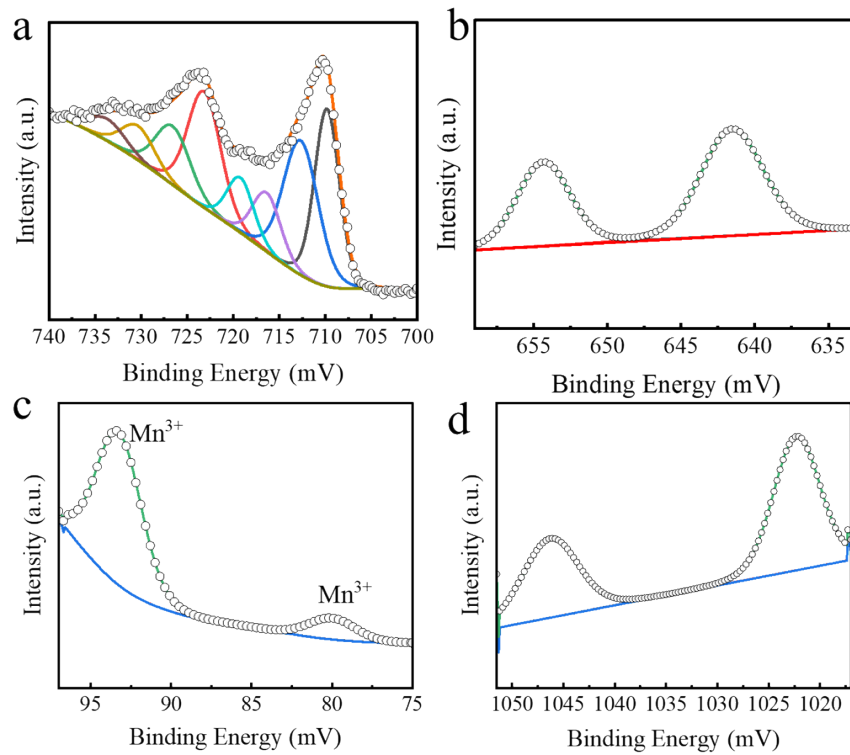Fig. S3 XRD patterns of MZF-C NFs. High-resolution XPS spectra of (j) Fe2p, (k) Mn2p, (l) Mn3s, and (m) Zn2p.

Fig. S4 XRD patterns of MZF-NFN. High-resolution XPS spectra of (j) Fe2p, (k) Mn2p, (l) Mn3s, and (m) Zn2p.
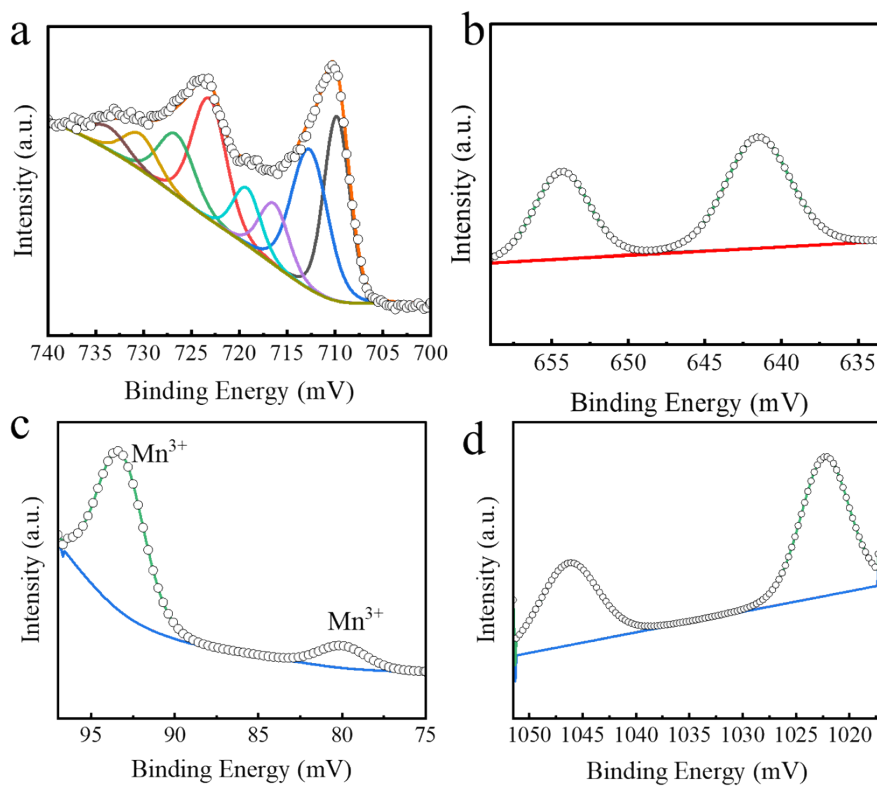

Fig. S5 XRD patterns of MZF-HS. High-resolution XPS spectra of (j) Fe2p, (k) Mn2p, (l) Mn3s, and (m) Zn2p.
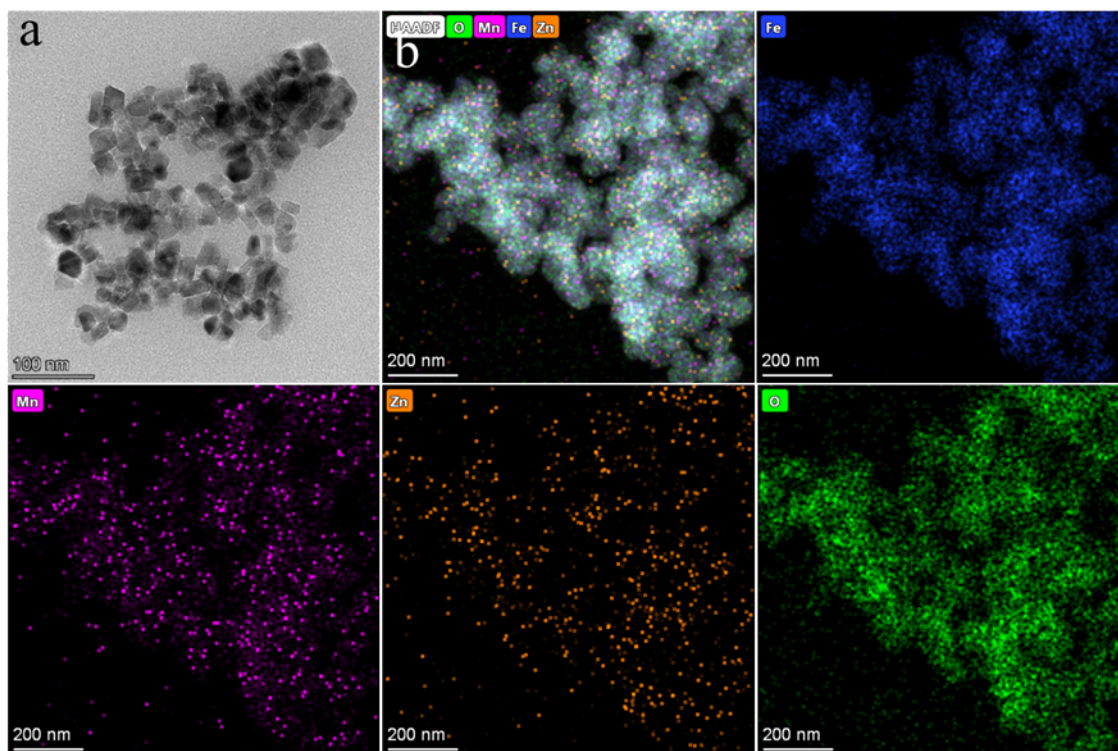
Fig. S6 (a) TEM image of MZF-C; (b) TEM-EDS elemental mapping images of an individual MZF-C
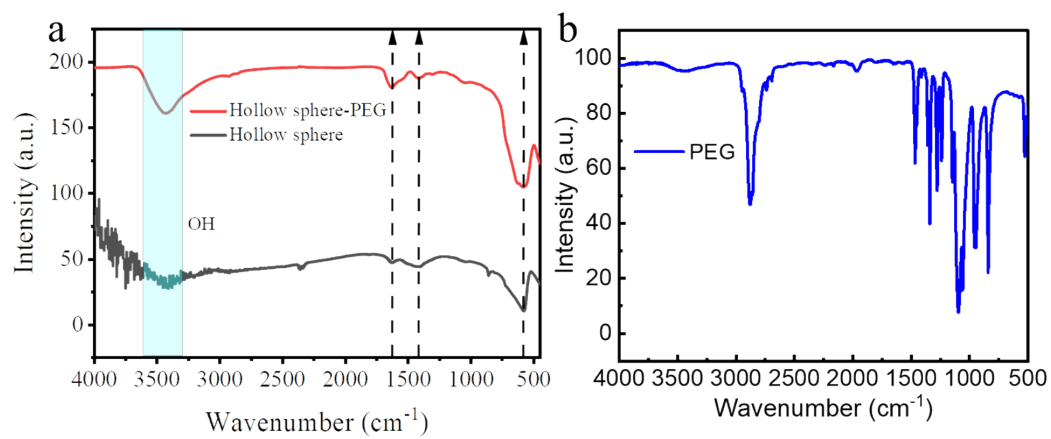

Fig. S7 FTIR spectra of (a) MZF-HS and MZF-HS-PEG, (b) PEG
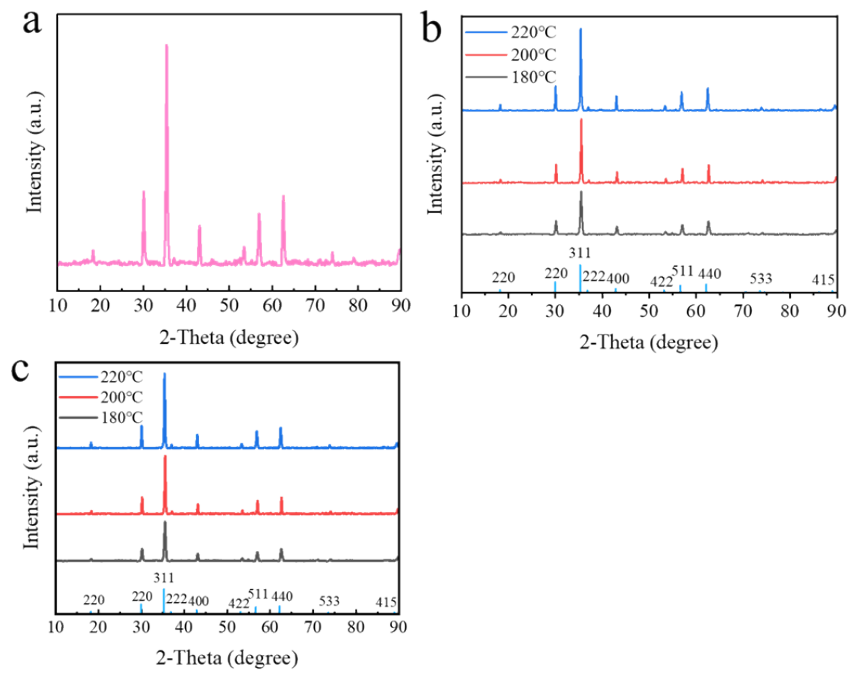
Fig. S8 (a) XRD patterns of MZF-C; (b) XRD patterns of MZF-NFN; (c) XRD patterns of MZF-HS.
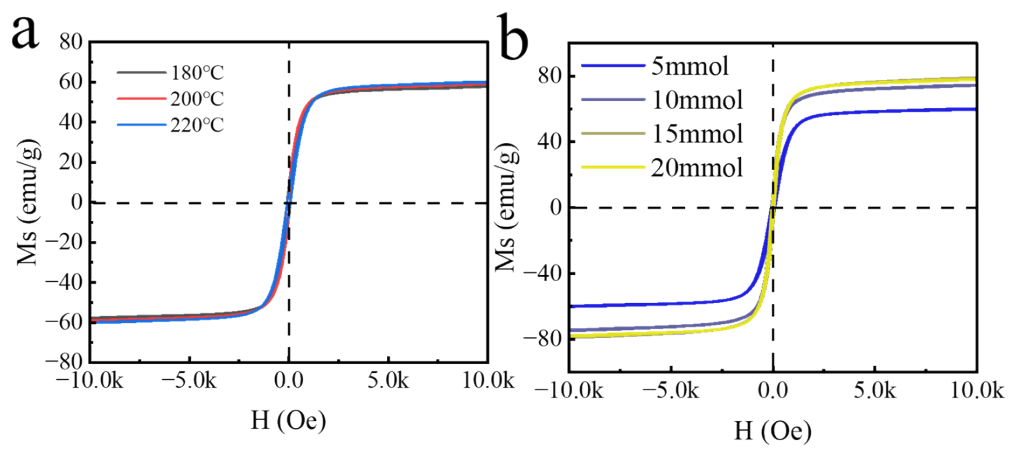

Fig. S9 (a)The *H-M* curves of MZF-HS at different solvothermal temperatures; (b) The *H-M* curves of MZF-NFE at different content of NaAc
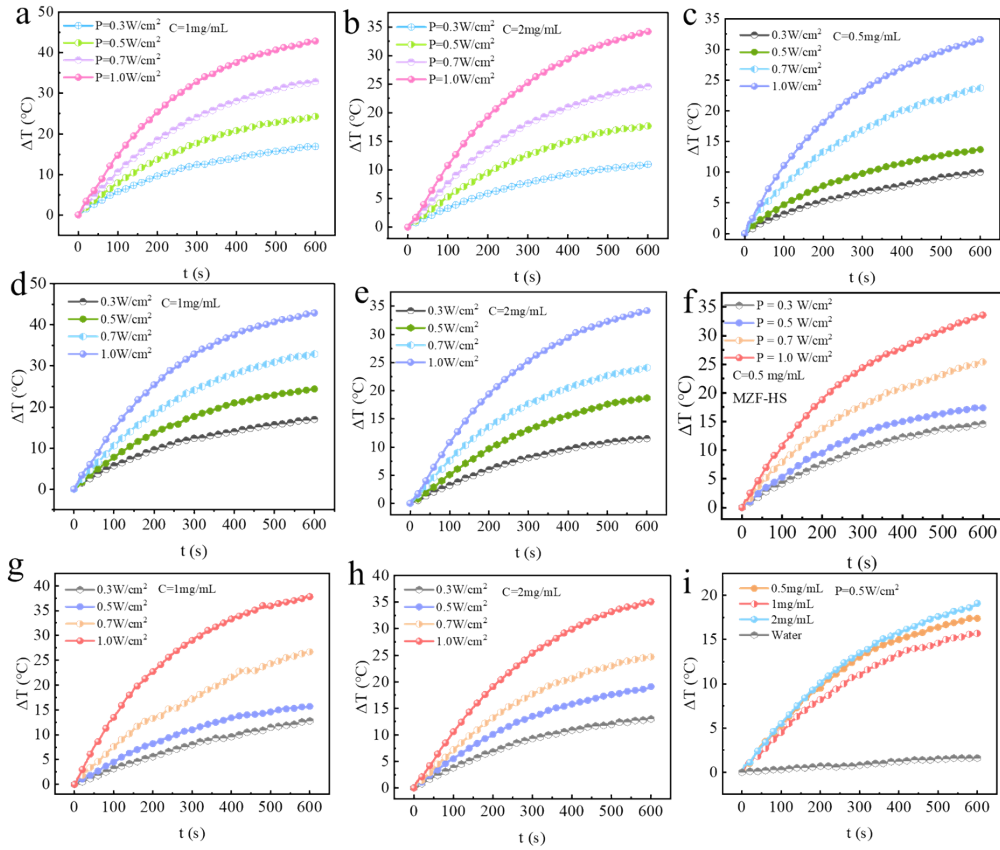
Fig. S10 Temperature elevation of MZF-NFE aqueous dispersion with a concentration of (a)1.0 mg mL^{-1}, (b) 2.0 mg mL^{-1} irradiated for 10 min under 808 nm laser with different power densities. Temperature elevation of MZF-NFN aqueous dispersion with a concentration of (c) 0.5 mg mL^{-1}, (d) 1.0 mg mL^{-1}, and (e) 2.0 mg mL^{-1} irradiated for 10 min under 808 nm laser with different power densities. Temperature elevation of MZF-HS aqueous dispersion with a concentration of (f) 0.5 mg mL^{-1}, (g) 1.0 mg mL^{-1}, (h) 2.0 mg mL^{-1} irradiated for 10 min under 808 nm laser with different power densities. (i) Temperature elevation of MZF-HS aqueous dispersion with different concentrations irradiated with 808 nm laser (0.5 W cm^{-2}) for 10 min.
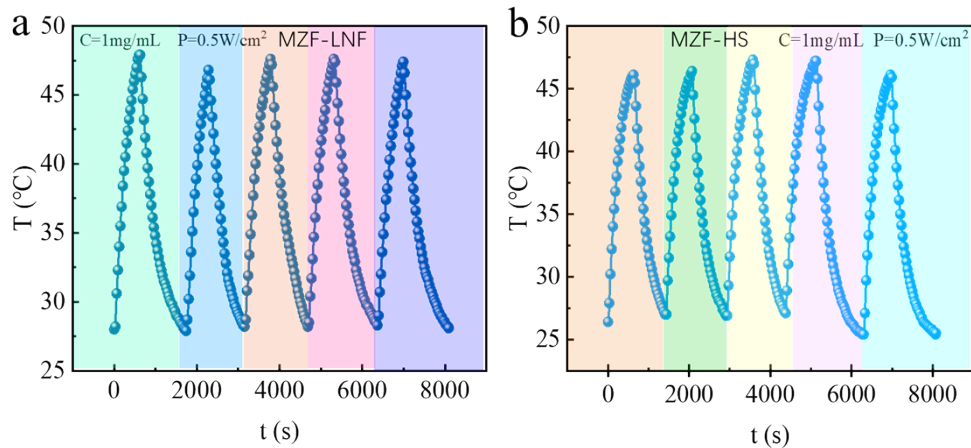
Fig. S11 (a) Recycling heating-cooling curve of MZF-NFE for five on/off rounds. (b) Recycling heating-cooling curve of MZF-HS for five on/off rounds.

Photothermal conversion efficiency

A theoretical model developed previously by Roper's method was employed to analyze the photothermal conversion process and determine the photothermal conversion efficiency η using the equation below:

$$\eta = \frac{B(T_{end} - T_0) + C(T_{end} - T_0)^2 - I\xi}{I(1 - \xi)(1 - 10^{-E})} \qquad (1)$$

where $I = 2.0$ W is the laser output power value, and E is the extinction value at 808 nm. B and C are two coefficients characterizing the temperature-dependent thermal loss of the entire system. They can be determined by fitting the temperature decay curve of the system recorded as a function of time after the laser is switched off. A representative temperature decay curve is given in Figure S5. T_0 is the temperature of the solution before the laser irradiation, and T_{end} is the steady temperature reached under the laser irradiation. ξ is the fraction of the laser energy absorbed by the cuvette walls and the solution. The value of ξ was determined by measuring the temperature rise and decay curves of pure water. In our experiment, ξ was found to be 0.039. According to Equation (1), we obtained a photothermal conversion efficiency (η) of MZF-HS, MZF-NFE, and MZF-NFN was calculated to be 24.7%, 20.3%, and 18.6%.
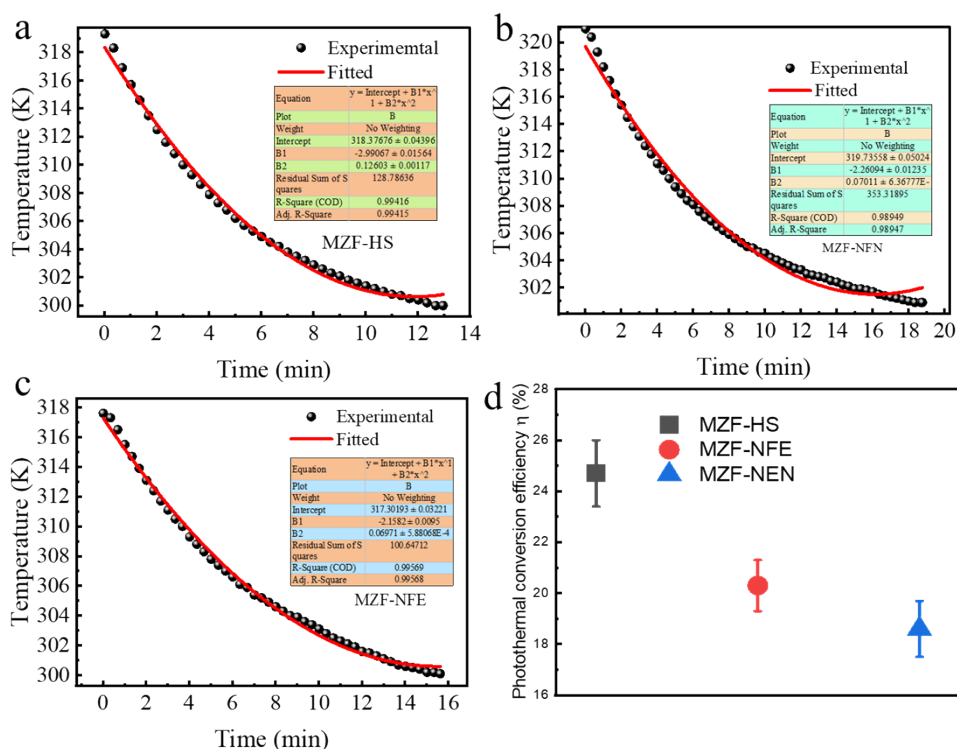
Fig. S12. Experimental (spheres) and fitted (solid line) temperature decay of (a) MZF-HS, (b) MZF-NFN, (c) MZF-NFE solution after the laser is switched off. (d) Photothermal conversion efficiency of different shapes MZF.

materials	concentration	laser power	efficiency	references
Ag@Au	100 μg mL^{-1}	2.0 W cm^{-2}	44.35%	1
branched Au superparticles	100 μg mL^{-1}	2.0 W cm^{-2}	91.0%	2
AuCu star/Cu$_{2-x}$S$_x$	50 μg mL^{-1}	0.5 W cm^{-2}	68.50%	3
Au@Ru	50 μg mL^{-1}	0.5 W cm^{-2}	54.14%	4
carbon framework/PVA	25000 μg mL^{-1}	10.0 W cm^{-2}	43.30%	5
PF700	5000μg mL^{-1}	0.52 W cm^{-2}	54.20%	6
Y-CQDs	200 μg mL^{-1}	1.0 W cm^{-2}	32.60%	7
CuS NPs	200 μg mL^{-1}	1 .0 W cm^{-2}	28.51%	8
MoS$_2$ nanosheets	250 μg mL^{-1}	1.5 W cm^{-2}	35.13%	9
Zn$_x$Mn$_{1-x}$Fe$_2$O$_4$@SiO$_2$:zNd^{3+}	500 μg mL^{-1}	1.5 W cm^{-2}	24%	10
This work MZF-HS	1000 μg mL^{-1}	1.0 W cm^{-2}	24.7%	
This work MZF-NFE	1000 μg mL^{-1}	1.0 W cm^{-2}	20.3%	

The photothermal conversion performances of Ag basic materials were higher than most of the

reported photothermal conversion materials of different kinds. Of course, there were also higher photothermal conversion efficiencies as the Au-based material prepared by Zhong et al.[2] Their branched Au particles also exhibited broad absorption and has a smaller particle size compared to our MZF-HS and MZF-NFE. Its good dispersion ability led to a slower cooling rate in the photothermal conversion process and further yielded a higher photothermal conversion efficiency (91.0%). Although MZF-HS and MZF-NFE prepared in this paper do not have higher photothermal conversion efficiency than plasmon and carbon-based materials, as non-radiative relaxation photothermal materials, they also have better magnetic properties and can produce more efficient heat under the effect of magneto-optical coordination.

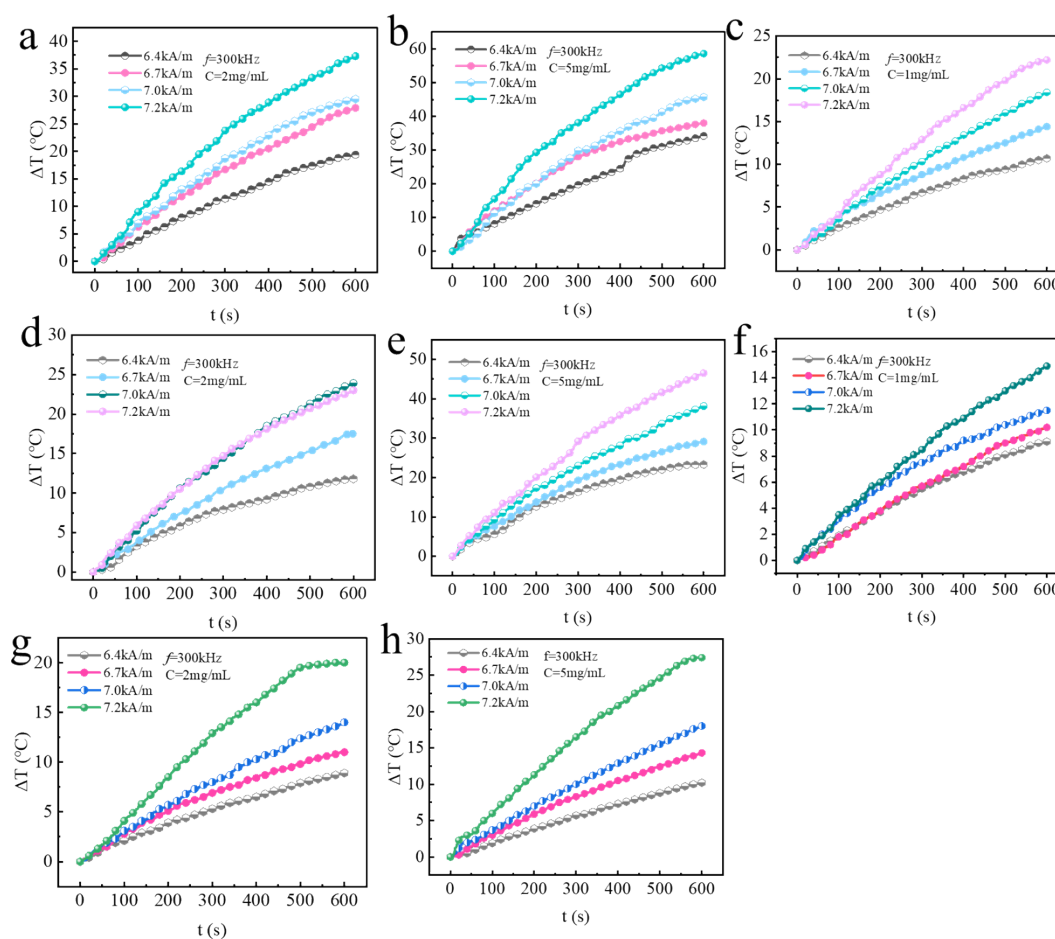Fig. S13 Heating profiles of MZF-NFL aqueous solution under AMF (f = 300 kHz, H = 6.4 kA/m to 7.2 kA/m) (a) 2 mg mL^{-1}, (b) 5 mg mL^{-1}. Heating profiles of MZF-NFN aqueous solution under AMF (f = 300 kHz, H = 6.4 kA/m to 7.2 kA/m) (a) 1 mg mL^{-1}, (b) 2 mg mL^{-1}, and (c) 5 mg mL^{-1}. Heating profiles of MZF-HS aqueous solution under AMF (f = 300 kHz, H = 6.4 kA/m to 7.2 kA/m)

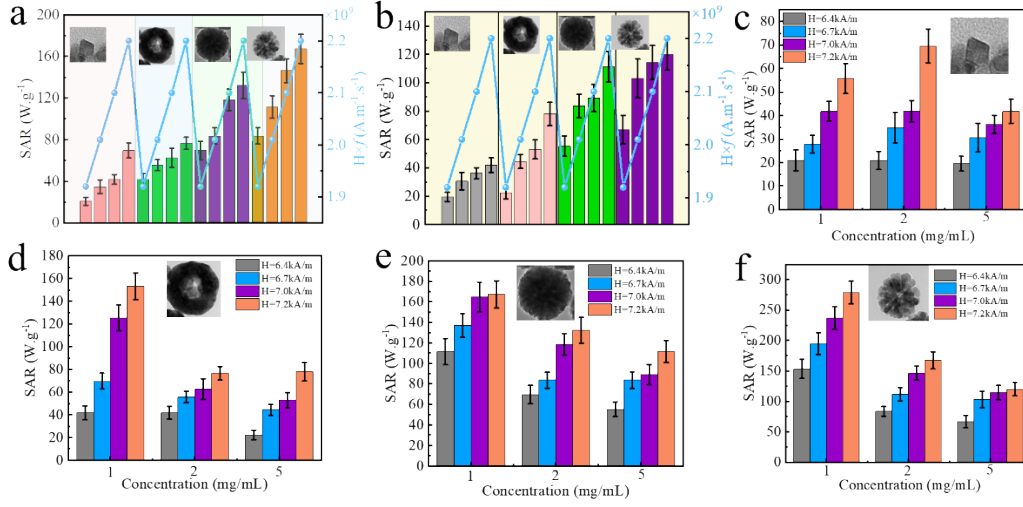(a) 1 mg mL^{-1}, (b) 2 mg mL^{-1}, and (c) 5 mg mL^{-1}.

Fig. S14 SAR values as a function of $H \times f$ product for the different shapes of MZF with the concentration of (a) 2 mg mL^{-1} and (b) 5 mg mL^{-1}. SAR values for (c) MZF-NFE, (d) MZF-HS, (e) MZF-NFN, and (f) MZF-NFE with different concentrations (1 mg mL^{-1}, 2 mg mL^{-1}, and 5 mg mL^{-1}) under an AC magnetic fields (H = 6.4 kA/m to 7.2 kA/m) at a constant frequency, f = 300 kHz.

Simulation method

The magnetization configurations and switching behaviors were studied numerically for multicore nanoflower, cube nanoparticles, and sphere nanoparticles. The detail size of those objects was described in SI Fig. The simulation was performed using Mumax3. In this software, the total energy (E_{tot}) of the magnet consists of four terms: Zeeman energy (E_{zee}), exchange energy (E_{ex}), anisotropy energy (E_{ani}), and demagnetizing energy (E_{demg}). The evolution of magnetization distribution was obtained by solving the Landau–Liftshitz–Gilbert (LLG) equation:[11]

$$\frac{\partial M(r,t)}{\partial t} = \gamma_G \big(M(r,t) \times H_{eff} \big) - \frac{\alpha_G}{M_s} M(r,t) \times H_{eff},$$

Where $M(r,t)$ is the magnetization distribution, H_{eff} is the effective field, M_s is the saturation magnetization, γ_G is the gyromagnetic ratio (1.78×10^7 s^{-1}Oe^{-1}), and α_G is the damping coefficient. The magnetic parameter of the three structures used in the micromagnetic simulation is listed as follows table:

Type Magnetization (Ms)	Exchange stiffness constant (A)	Magnetocrystalline anisotropy constant K_1	Damping coefficient α_G
A m^{-1}	J m^{-1}	J m^{-3}	-

Cube	220e3	1.3e-11	0	0.01
Hollow sphere	330e3	1.2e-11	0	0.5
Nanoflower	450e3	1.2e-11	0	0.5

In our simulation, the cell size is $2 \times 2 \times 2$ nm, which is smaller than the magnetostatic exchange length of Fe_3O_4 ($l_{ex} = \sqrt{2A/\mu_0 M_s^2} \approx 8\ nm$) to ensure the accuracy of the simulation.
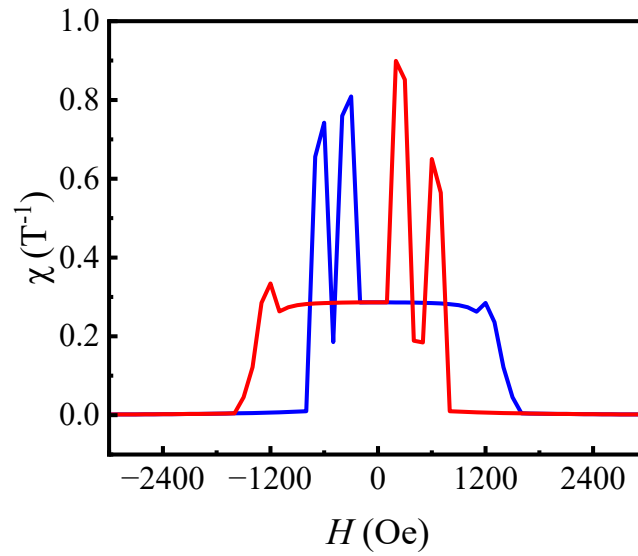

Fig. S15. *The differential magnetic susceptibility χ ($\chi = dM/dH$)) of MZF-HS according to Fig. 4d, the blue line is the ascending branch (-2500 Oe - 2500 Oe), and the red line is the descending branch (2500 Oe - -2500 Oe).*
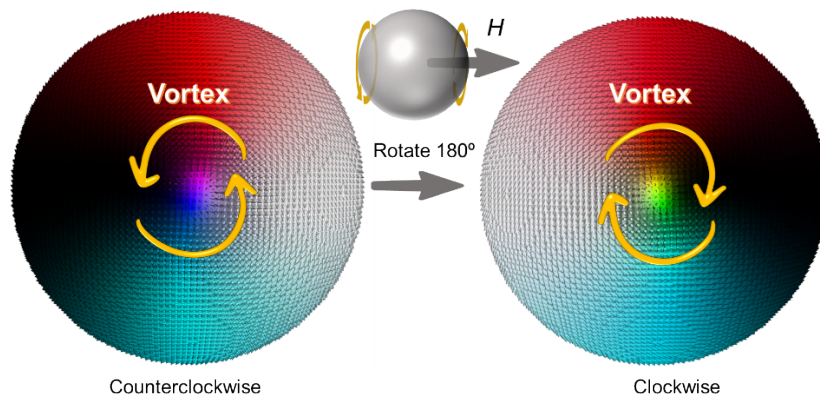

Fig. S16. The formation of a field-induced double vortex with a pair of counterclockwise and clockwise vortices

-1500 Oe   -600 Oe   -200 Oe   0 Oe   200 Oe   600 Oe   1500 Oe
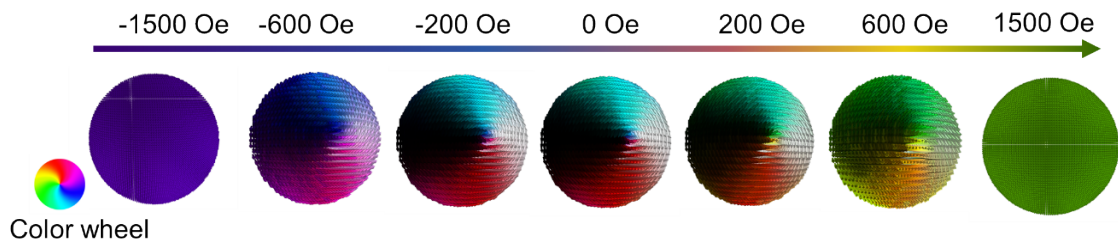
Color wheel

Fig. S17. The magnetization configuration for MZF-HS under external field sweep.
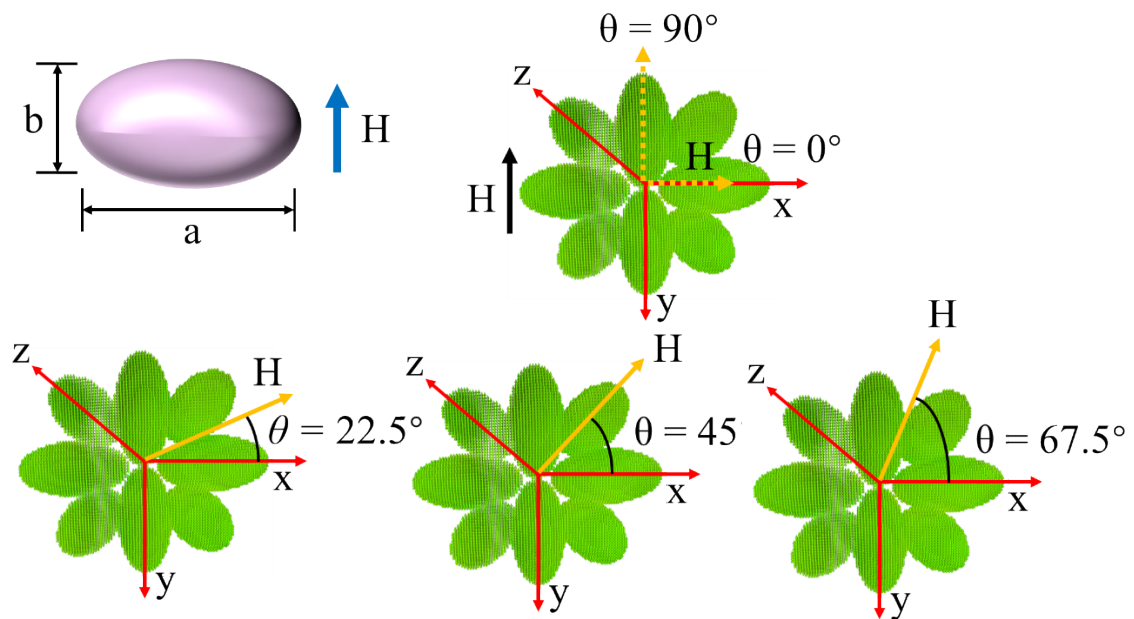

Fig. S18 Schematic of the geometry and 3D coordinate system of the magnetic core of MZF-NFE;

the external magnetic field is applied along the different angles θ (0°, 22.5°, 45°, 67.5°, and 90°).

θ = 0°   θ = 22.5°   θ = 45°

θ = 67.5°   θ = 90°
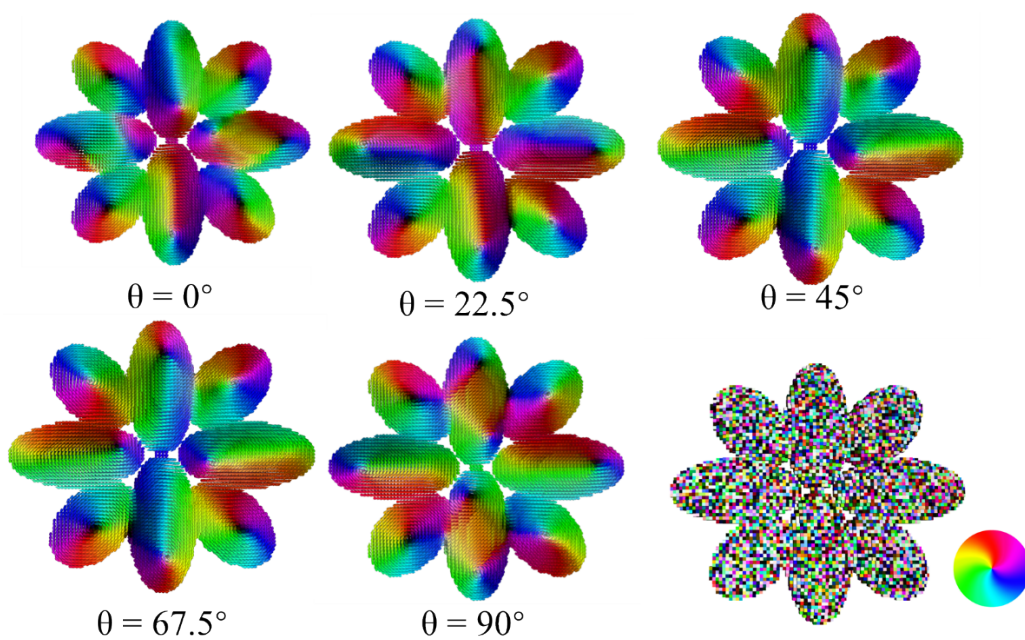
Fig. S19 The remanence magnetization configurations of MZF-NFE with varying magnetic field angle θ from 0° to 90°. And MZF-NFE ferrimagnets with random initial magnetization modeled in the micromagnetic simulation.
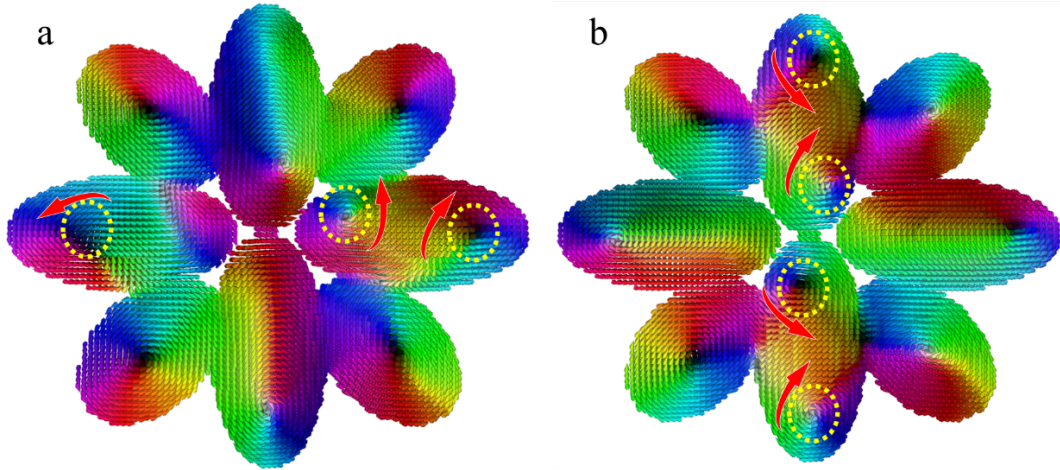
Fig. S20 The magnetization configuration of MZF-NFE at the external alternating magnetic field (100 Oe) with the angle of (a) 0° and (b) 90°.

Fig. S21 The plot of (a) demagnetization energy, (b) exchange energy, (c) Zeeman energy, and (d) total energy against applied magnetic field H.

Fig. S22 Simulated magnetization configuration of the MZF-NFE at 100 Oe (θ = 0°)

Mathematical model for simulation

To investigate the impact of a solenoid-generated magnetic field on temperature distribution during magnetic hyperthermia, we conducted simulations using COMSOL Mul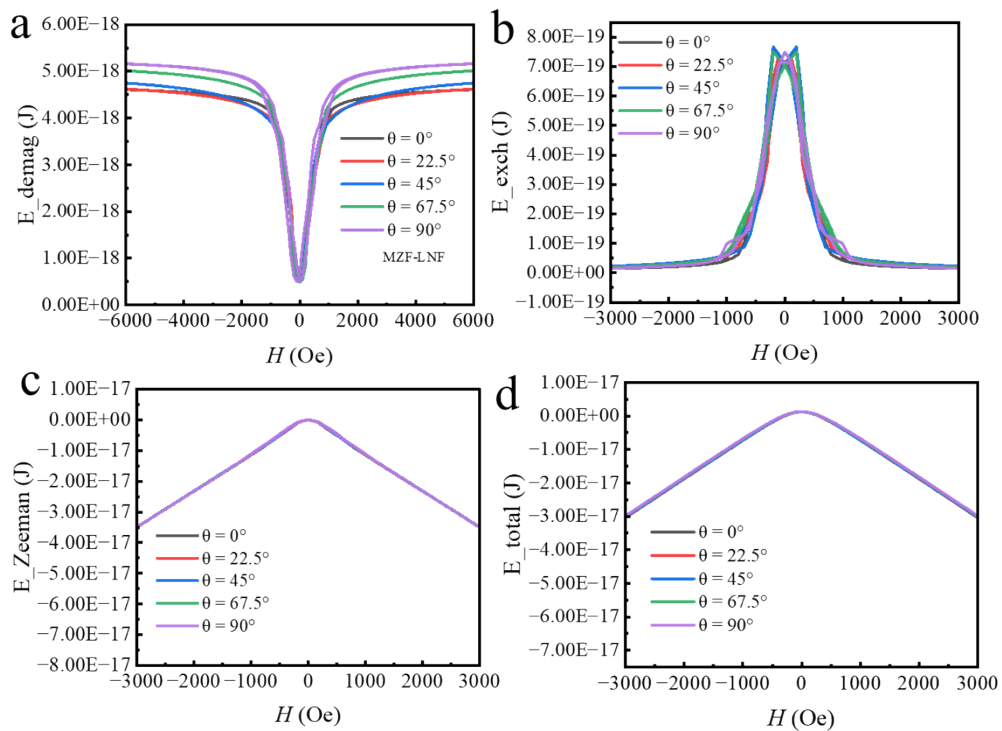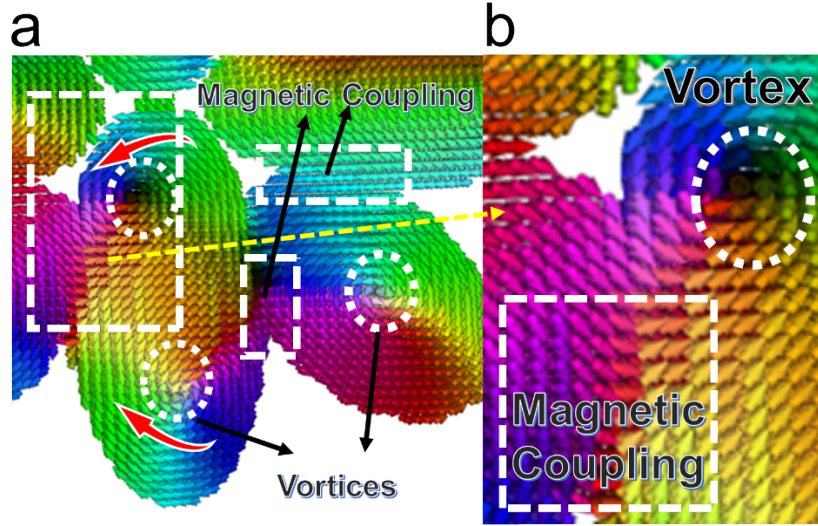tiphysics to solve the bio-heat transfer equation. The therapeutic target was positioned entirely within the solenoid, which had a diameter of 45 mm and 3 turns. The target consisted of healthy tissue (30 mm in diameter) and a tumor (10 mm in diameter). To facilitate comprehension, we categorized the model's equations into three groups: those describing the magnetic field produced by the solenoid, the power dissipation of MNPs, and the temperature field in the tumor region. In this section, we present and describe each group, beginning with the equations that describe the magnetic field. When an alternating current is applied to the solenoid, it generates a magnetic field both around and inside it, following Maxwell's theory, which can be expressed in its differential form as the generalized Ampere's law.

$$\nabla \times H = J + \frac{\partial D}{\partial t},$$
(3)

In this context, H represents the magnetic field strength, J denotes the free current density, D signifies the electric displacement field, and t stands for time. The magnetic field strength, H, can be expressed as a function of the magnetic flux density, B, in the following manner,

$$H = \mu_0^{-1} B,$$
(4)

where $\mu_0 = 4\pi \cdot 10^{-7} \, T \cdot m \cdot A^{-1}$ is the permeability of free space. Furthermore, the magnetic flux density can be expressed in terms of the magnetic vector potential, A, as

$$B = \nabla \times A, \qquad (5)$$

the electric displacement vector field is defined as:

$$D = \varepsilon_0 E + P_{E'} \qquad (6)$$

where $\varepsilon_0 = 8.85 \cdot 10^{-12} F \cdot A^{-1}$ is the permittivity of free space, E denotes the induced electric field, while PE represents the polarization density, which is considered to be negligible as the model in this paper does not account for any dielectric material. The induced electric field, E, can be correlated to the free current density by utilizing the generalized Ohm's law:

$$J = J^e + \sigma E, \qquad (7)$$

where J^e denotes the current density due to an external current and $\sigma = 1.46 \cdot 10^7 S \cdot m^{-1}$ is the electrical conductivity. Moreover, in a stationary system, according to Maxwell-Faraday equation, , E can be written as:

$$E = -\frac{\partial A}{\partial t} - \nabla \varphi, \qquad (8)$$

In this model, the scalar potential φ is assumed to be zero, as there are no aggregated charges. By substituting Eqs. (2) and (6) into Eq. (1), we derive a final partial differential equation that establishes the relationship between the magnetic vector potential and the external current density, as shown in Eq. (8). This equation can be effectively solved through the finite element method, enabling the determination of the magnetic field strength using the resulting magnetic vector potential obtained from Eq. (4).

$$\varepsilon_0 \frac{\partial^2 A}{\partial t^2} + \sigma \frac{\partial A}{\partial t} + \nabla \times \mu_0^{-1}(\nabla \times A) = J^e \qquad (8)$$

The power dissipation of magnetic nanoparticles per unit volume within each region of the model can be accurately described by Rosensweig's theory, taking into account the magnetic field characteristics of the nanoparticles:

$$P = \pi \mu_0 H_m f \chi'', \qquad (9)$$

Here, P represents the power dissipation of particles per unit volume. Hm and f denote the magnitude and frequency of the magnetic field applied to the magnetic nanoparticles, respectively. Additionally, χ" represents the imaginary part of the complex magnetic susceptibility, which can be expressed as:

$$\chi'' = \frac{\mu_0 M_s^2 V_M}{3k_B T_0} \frac{2\pi f \tau}{1 + (2\pi f \tau)^2}, \quad (10)$$

Here, M_s represents the saturation magnetization of the magnetic nanoparticles, V_M denotes the volume of each particle, k_B stands for the Boltzmann constant, T_0 represents the absolute temperature of the magnetic particles, and τ indicates the relaxation time of the magnetic nanoparticles. Upon determining the thermal energy of the magnetic nanoparticles, the temperature distribution in the bio-tissue can be obtained by solving Pennes' bio-heat transfer equation.

The magnetic particles are selectively placed within the tumor tissue, with no presence in the surrounding healthy tissue. Consequently, the present study employs two coupled bio-heat transfer equations to predict the temperature distribution—one for the tumor region and the other for the healthy tissue region:

$$\rho_1 c_1 \frac{\partial T_1}{\partial t} = \nabla(k_1 \nabla T_1) - \omega_{b1} c_{b1}(T_1 - T_b) + Q_{m1} + P, \ \gamma \leq R, \quad (11)$$

$$\rho_2 c_2 \frac{\partial T_2}{\partial t} = \nabla(k_2 \nabla T_2) - \omega_{b2} c_{b2}(T_2 - T_b) + Q_{m2}, \ \gamma > R, \quad (12)$$

The subscripts 1 and 2 indicate the parameters of the tumor region and the healthy region, respectively. ρ represents the density of the tissue, c denotes the specific heat of the tissue, and k stands for the heat conductivity of the tissue. Additionally, ω_b represents the blood perfusion rate, T_b signifies the temperature of blood (37 °C), and Q_m represents the metabolic heat per unit volume.

The properties of the tumor domain are influenced by the volume fraction of magnetic nanoparticles injected into the tumor. In the tumor region, the values of ρ, c, and k are considered to be [12]:

$$\rho_1 = (1 - \varphi)\rho_T + \varphi \rho_{MNP},$$

$$c_1 = (1 - \varphi)c_T + \varphi c_{MNP},$$

$$\frac{1}{k_1} = \frac{1 - \varphi}{k_T} + \frac{\varphi}{k_{MNP}},$$

In this context, the subscript T denotes the original properties of the tumor, while MNP represents the properties of the magnetic nanoparticles. Both sets of properties are listed in Table 1.

Table 1 Physical parameters for solving the heat transfer equation [13].

Tissue	Density	Specific heat	Thermal conductivity	Conductivity	Relative permittivity	Blood perfusion	Metabolic heat rate
	$\rho[kg\,m^{-3}]$	$C_p[J\,kg^{-1}K^{-1}]$	$k[W\,m^{-1}K^{-1}]$	$\sigma[S m^{-1}]$	$\varepsilon_r[1]$		$w_b[S^{-1}]$

$Q_{met}[W\,m^{-3}]$							
Liver	1064	3500	0.50	0.35-0.52	1.53E3-1.0E4	6.72E-4	922
Tumor	1050	3540	0.50	0.35-0.52	1.53E3-1.0E4	8.33E-4	5790
Blood	1050	3617	0.52	0.7-0.85	2.6 E3-5.2E3	-	-
Magnetic fluid	1200	3800	0.65	1.5	1	-	-
Water	1000	4178	0.6	5.7E-10	84.64	-	-

Thermal damage assessment

After determining the treatment temperature for the model, the malignant cells can be effectively damaged when subjected to this specific temperature. Simultaneously, the evaluation of thermal damage in tissue was conducted through a first-order thermal-chemical rate equation coupled with the Pennes bioheat equation, which simulated the temperature field. The mortality of malignant cells is closely linked to the appropriate treatment temperature, but it is also significantly influenced by the kinetic coefficients of the Arrhenius model during the magnetothermal treatment. The extent of thermal damage at a specific location (x, y, z) is determined by the temperature-time history, which is quantified using a parameter, Ω, calculated by the Arrhenius equation [13]:

$$\Omega(x,y,z,t) = In\left[\frac{\zeta(0)}{\zeta(t)}\right] = exp\left(\int_0^t k\,dt\right) \tag{13}$$

$$k(t) = A\,exp(-E_a/R_u T_t(x,y,z,t)) \tag{14}$$

Where $\zeta(0)$ is the initial concentration of normal cells, $\zeta(t)$ is the concentration of normal cells remaining after heating of a duration $t(s)$, $k(t)$ is the cell injury rate, A is the frequency factor for the damage process $(1/s)$, E_a is the activation energy(J/mol), R_u is the universal gas constant (8.23 J/mol K). Kinetic parameters, E_a and A, must be determined before solving the Arrhenius model using experimental data. In the present study, the temperature dependency of the E_a and A for PC3 cells was listed in Table 1, which is from the previous study [14].

Table 2

Arrhenius parameters for PC3 tumors [14]

Parameter	Symbol	Temperature (℃)	PC3 Cells	Tissue
Frequency factor (1/s)	A	$T \leqslant 54$	1.8×10^{36}	6.36×10^{19}
		$T \geqq 54$	7.0×10^{17}	-

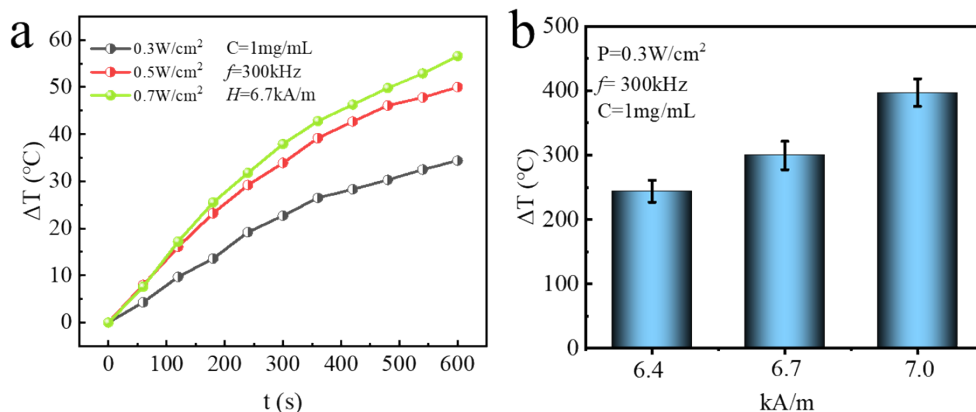| Activation energy (J/mol)	E_a	$T{\le}54$	2.38×10^5	1.38×10^5
		$T{\ge}54$	1.24×10^5	-

Fig. S23 (a) Heating curves for the MZF-NFE under different laser powers and a constant magnetic field frequency, f = 300 kHz, and H = 6.7 kA/m irradiated for 10 min. (b) SAR values of MZF-NFE (1 mg mL^{-1}) as a function of H under a constant NIR laser power of 0.3 W/cm^2.

1. W. Liu, Y. Wang, Y. Wang, X. Li, K. Qi, J. Wang and H. Xu, ACS Appl Mater Interfaces, 2022, DOI: 10.1021/acsami.2c14436.

2. Zhong, Q.; Feng, J.; Jiang, B.; Fan, Y.; Zhang, Q.; Chen, J.; Yin, Y. Strain-Modulated Seeded Growth of Highly Branched Black Au Superparticles for Efficient Photothermal Conversion. J. Am. Chem. Soc. 2021, 143, 20513−20523.

3. Yu, Q.; Peng, T.; Zhang, J.; Liu, X.; Pan, Y.; Ge, D.; Zhao, L.; Rosei, F.; Zhang, J. Cu2-xSx Capped AuCu Nanostars for Efficient Plasmonic Photothermal Tumor Treatment in the Second NearInfrared Window. Small 2022, 18, 2103174.

4. Ji, L.; Zhang, L.; Yang, H.; Liang, S.; Pan, J.; Zou, Y.; Li, S.; Li, Q.; Zhao, S. Versatile Au@Ru Nanocomposites for the Rapid Detection of Salmonella Typhimurium and Photothermal Sterilization. J. Colloid Interface Sci. 2022, 621, 489−498.

5. Zhang, X.; Cheng, P.; Song, W.; Rong, S.; Huang, J.; Wang, D.; Schaaf, P.; Zhou, G.; Zhang, Z.; Liu, J. Photo-Thermoelectric Conversion and Photo-Induced Thermal Imaging Using 2D/3D ReS2@Carbon Framework with Enhanced Photon Harvesting. Chem. Eng. J. 2022, 446, 137084.

6. Wei, C.; Jin, X.; Wu, C.; Brozovic, A.; Zhang, W. Carbon Spheres with High Photothermal Conversion Efficiency for Photothermal Therapy of Tumor. Diamond Relat. Mater. 2022, 126,

109048.

7. Moniruzzaman, M.; Deb Dutta, S.; Lim, K.-T.; Kim, J. Wet Chemistry-Based Processing of Tunable Polychromatic Carbon Quantum Dots for Multicolor Bioimaging and Enhanced NIRTriggered Photothermal Bactericidal Efficacy. Appl. Surf. Sci. 2022, 597, 153630.

8. Li, J.; Cheng, Q.; Yue, L.; Gao, C.; Wei, J.; Ding, Y.; Wang, Y.; Zheng, Y.; Wang, R. Macrophage-Hitchhiking Supramolecular Aggregates of CuS Nanoparticles for Enhanced Tumor Deposition and Photothermal Therapy. Nanoscale Horiz. 2021, 6, 907−912.

9. Liu, J.; Lu, K.; Gao, F.; Zhao, L.; Li, H.; Jiang, Y. Multifunctional MoS2 Composite Nanomaterials for Drug Delivery and Synergistic Photothermal Therapy in Cancer Treatment. Ceram. Int. 2022, 48, 22419−22427.

10. M. Vinícius-Araújo, N. Shrivastava, A. A. Sousa-Junior, S. A. Mendanha, R. C. D. Santana and A. F. Bakuzis, ACS Applied Nano Materials, 2021, 4, 2190-2210.

11. Vansteenkiste, A.; Leliaert, J.; Dvornik, M.; Helsen, M.; Garcia-Sanchez, F.; Van Waeyenberge, B., The design and verification of MuMax3. *AIP Advances* **2014,** *4* (10).

12. I. Astefanoaei, I. Dumitru, H. Chiriac, S. Alexandru, Thermofluid analysis in magnetic hyperthermia using low Curie temperature particles, IEEE Trans. Magn. 52 (2016) 1–5.

13. Y. Tang, T. Jin, R.C.C. Flesch, Numerical Temperature Analysis of Magnetic Hyperthermia Considering Nanoparticle Clustering and Blood Vessels, IEEE Transactions on Magnetics 53(10) (2017) 1-6.

14. A. LeBrun, R. H. Ma, L. Zhu, Micro CT image based simulation to design heating protocols in magnetic nanoparticle hyperthermia for cancer treatment, Journal of Thermal Biology. 62(2016)129-137.